

Materials Advances

Accepted Manuscript

This article can be cited before page numbers have been issued, to do this please use: X. Yang, M. Alhabradi, A. Roy, M. Alruwaili, D. Benson, H. Chang, X. Li, A. A. Tahir and Y. Zhu, *Mater. Adv.*, 2026, DOI: 10.1039/D5MA01065A.



This is an Accepted Manuscript, which has been through the Royal Society of Chemistry peer review process and has been accepted for publication.

Accepted Manuscripts are published online shortly after acceptance, before technical editing, formatting and proof reading. Using this free service, authors can make their results available to the community, in citable form, before we publish the edited article. We will replace this Accepted Manuscript with the edited and formatted Advance Article as soon as it is available.

You can find more information about Accepted Manuscripts in the [Information for Authors](#).

Please note that technical editing may introduce minor changes to the text and/or graphics, which may alter content. The journal's standard [Terms & Conditions](#) and the [Ethical guidelines](#) still apply. In no event shall the Royal Society of Chemistry be held responsible for any errors or omissions in this Accepted Manuscript or any consequences arising from the use of any information it contains.

Enhancing the Uniformity of CuBi₂O₄ Thin Film for Photoelectrochemical (PEC) Water Splitting through Urea-Modified Ethylene Glycol Electrolyte

Xiuru Yang^a, Mansour Alhabradi^{bc}, Anurag Roy^b, Manal Alruwaili^{bd}, David Benson^b, Hong Chang^a, Xiaohong Li^b, Asif Ali Tahir^{*b}, Yanqiu Zhu^{*a}

^{*}Corresponding authors

^a Faculty of Environment, Science and Economy, University of Exeter, Exeter EX4 4QF, UK

^b Faculty of Environment, Science and Economy, University of Exeter, Penryn TR10 9FE, UK

^c Department of Physics, Faculty of Science, Majmaah University, Majmaah, 11952, Saudi Arabia

^d Department of Physics, Faculty of Science, Jouf University, 2014, Sakaka 42421, Saudi Arabia

E-mail: Y.Zhu@exeter.ac.uk



Abstract

View Article Online
DOI: 10.1039/D5MA01065A

CuBi₂O₄ photocathode with interconnected nanoparticle textured morphology has reached a photocurrent density of -0.94 mA/cm² at 0.52 V vs. RHE. It was successfully fabricated via electrodeposition using ethylene glycol (EG) containing a specific concentration of Bi(NO₃)₃·5H₂O and CuCl₂ as the electrolyte, followed by 2 h of calcination at 550 °C. Using urea as a complexing agent in the EG electrolyte enhanced the photocurrent density of the CuBi₂O₄ photocathode. Adding 0.15 g of urea to the electrodeposition solution improved film uniformity, enhanced PEC water splitting efficiency, and achieved a photocurrent density of -1.44 mA/cm² at 0.52 V vs. RHE. This value is higher than those of previously reported CuBi₂O₄ photocathodes, which typically exhibit photocurrent densities below -1.0 mA/cm². To understand the factors contributing to this enhanced PEC performance, this study investigated the effects of varying urea concentrations (0, 0.1, 0.15, and 0.2 g per 100 mL EG) on the crystallite domain size, morphology, surface roughness, light absorption, band gap, electronic band structure, and PEC performance. A mechanism was proposed to account for the long-term stability based on its inadequate valence band potential and irreversible degradation behaviour. This work provides insights for optimizing CuBi₂O₄ thin films to enhance their stability and efficiency in PEC water splitting applications.

Keyword: CuBi₂O₄; Electrodeposition; PEC water splitting; Photocathode; P-type semiconductor



1 Introduction

2 Photoelectrochemical (PEC) water splitting, which can directly convert solar energy to
3 hydrogen, has been identified as a critical alternative for developing a more efficient,
4 sustainable, and environmentally friendly future energy system. Efficient PEC hydrogen
5 generation relies heavily on the development of suitable photocathodes. Materials such as Si,¹
6 GaAs,¹ CuO,² Cu₂O,³ LaFeO₃,⁴ CuInS₂,⁵ CuFeO₂,⁶ Sb₂Se₃,⁷ InP,⁸ and Cu₂ZnSnS₄⁹ have been
7 explored due to their conduction band potentials being more negative than the H⁺/H₂ reduction
8 potential ($E(\text{H}^+/\text{H}_2) = 0 \text{ V vs. RHE}$),^{10,11} enabling energy-efficient hydrogen evolution. Among
9 p-type semiconductors, CuBi₂O₄ has attracted significant attention as a photocathode owing to
10 its low bandgap energy (1.5-1.8 eV) and favorable band structure, which predicts photocurrent
11 density of 19-27 mA/cm² under standard solar illumination (AM 1.5G, 100 mW/cm²).^{12,13}
12 However, practical application of CuBi₂O₄ thin films is significantly hindered by their intrinsic
13 limitations such as low charge carrier transfer kinetics, rapid recombination of photogenerated
14 charge carriers, and susceptibility to photocorrosion. Achieving high-quality thin films with
15 uniform thickness, controlled morphology, and strong adhesion to substrates remain essential
16 for improving the overall performance of CuBi₂O₄ thin films.

17 Various techniques, including spin coating,^{14,15} pulsed laser deposition (PLD),^{16,17}
18 physical vapor deposition (PVD) techniques (sputtering and electron beam evaporation),¹⁸⁻²⁰
19 doctor blade coating,^{21,22} spray pyrolysis,^{23,24} chemical bath deposition,^{25,26} and
20 electrodeposition,^{27,28} have been used to fabricate CuBi₂O₄ thin films. Among these,
21 electrodeposition is particularly attractive due to its low cost, mild operating temperature, and
22 ability to produce adherent interfaces, making it highly suitable for the creation of durable thin
23 films. However, non-uniform electrodeposition can reduce film quality and photocathode
24 performance. To address these issues, various strategies have been explored, including
25 adjusting the metal-ion concentration, implementing pH control through buffering, and adding
26 organic additives during the deposition process. Nakabayashi et al. improved the uniformity of
27 CuBi₂O₄ thin films by using tartrate ions to stabilize the Cu²⁺ and Bi³⁺ in solution. This
28 stabilization enabled controlled co-deposition of CuO and Bi₂O₃ at a high anodic potential.²⁹
29 After annealing at 500 °C, the resulting CuBi₂O₄ thin films exhibited enhanced coverage,
30 stronger adhesion, and better uniformity. Similarly, Hahn et al. prepared Cu-Bi
31 electrodeposition baths by dissolving Bi³⁺ and Cu²⁺ in 10% nitric acid. This step was essential
32 for fully dissolving bismuth nitrate and producing a homogeneous electrolyte, which is critical
33 for consistent electrodeposition.²⁷ The homogeneous bath enabled effective cathodic co-
34 deposition and subsequent annealing yield well-crystallized CuBi₂O₄ thin films. Citric acid has



also been employed as a complexing agent in CuBi_2O_4 synthesis. By forming stable metal-ligand complexes, it regulates the release of metal ions during electrodeposition, thereby promoting uniform film growth.³⁰

Urea is a small, inexpensive, and environmentally friendly molecule with strong hydrogen-bonding and coordination abilities.³¹⁻³³ Its $-\text{NH}_2$ group can donate hydrogen bonds while its carbonyl oxygen can accept them, enabling interactions with solvent molecules and metal ions.³¹⁻³³ These interactions tune the solvation environment, improve ion dissolution, and influence key solution properties such as ionic conductivity and viscosity, ultimately promoting uniform metal deposition and controlled thin-film growth.^{31,34,35} Motivated by these advantages, this work investigates the effect of urea at varying concentrations (0, 0.1, 0.15, and 0.2 g per 100 mL of ethylene glycol, EG) on the synthesis of CuBi_2O_4 thin film on FTO glass. The resulting thin films are systematically characterized in terms of crystallite size, morphology features, surface roughness, electronic band structures, and the PEC performance. Based on the observed enhancements, a potential mechanism involving charge separation and transfer is proposed to account for the enhancements in PEC performance.

Experimental Procedures

Materials and chemicals

The following chemicals were purchased and utilised without additional purification: Bismuth (III) nitrate pentahydrate ($\text{Bi}(\text{NO}_3)_3 \cdot 5\text{H}_2\text{O}$, 98%, Thermo Scientific Chemicals), Copper (II) chloride dihydrate ($\text{CuCl}_2 \cdot 2\text{H}_2\text{O}$, 99+%, ACS reagent, Thermo Scientific Chemicals), Sodium hydroxide (NaOH, 98%, extra pure, pellets, Acros Organics), and urea ($\text{CH}_4\text{N}_2\text{O}$, ultra-pure UPS grade, Melford). Ethylene glycol (EG, $\text{C}_2\text{H}_6\text{O}_2$, 99%, Thermo Scientific Chemicals) was used as the electrolyte for electrodeposition.

CuBi_2O_4 thin film preparation

A standard three-electrode system, consisting of a Pt counter electrode, an FTO working electrode, and an Ag/AgCl (4 M KCl) reference electrode, was used for the electrodeposition process. The FTO glass was electrically connected by placing copper tape on its edge with copper tape to ensure uniform current distribution when clipped with the Autolab tweezer during electrodeposition. A 100 mL EG solution comprising 6 mM $\text{Bi}(\text{NO}_3)_3 \cdot 5\text{H}_2\text{O}$, 3 mM CuCl_2 , and various amounts (0 g, 0.1 g, 0.15 g, and 0.2 g) of urea was utilised as the plating solution to create the Cu/Bi bimetallic films. The material was deposited by passing -0.06 C per cycle at a fixed potential of $E = -1.8$ V versus Ag/AgCl.¹⁰ After six rounds of this cycle by



accumulating a total charge of -0.36 C, the resulting Cu/Bi films were heated for 2 h at 550 °C in air with a ramping rate of 5 °C/min to produce the CuBi₂O₄ thin films. The samples were labelled as 0.1 g-urea-6C-9mM, 0.15 g-urea-6C-9mM and 0.2 g-urea-6C-9mM, respectively. As a reference, a sample generated using the same process but without adding urea into the EG electrolyte was labelled as 0 g-urea-6C-9mM.

PEC measurements

The Metrohm Autolab (PGSTAT302N) electrochemical workstation with a three-electrode compartment was used for all PEC analyses of the thin films. Platinum served as the counter electrode, Ag/AgCl (4 M KCl) as the reference electrode, and thin film as the working electrode, with 0.1 M NaOH at a pH of 12.8 as the electrolyte. A Newport 66902, 300 W xenon lamp with an air mass (AM) of 1.5 was used to approximate a light intensity of 100 mW/cm² (1 sun condition). The photocurrent density vs. $E_{\text{Ag/AgCl}}$ curves (J - V plots) were obtained by using the linear sweeping voltammetry (LSV) mode at a constant scan rate of 10 mV/s from -0.50 to 0.2 V vs Ag/AgCl. At a bias potential of -0.45 V vs Ag/AgCl, the electrochemical impedance spectroscopy (EIS) curves were recorded with a frequency range of 100 kHz to 0.1 Hz under a modulation amplitude of 10 mV. To compare with literature results, the experimental potential measured versus the Ag/AgCl reference electrode ($E_{\text{Ag/AgCl}}$) was converted to the potential versus the reversible hydrogen electrode (E_{RHE}) via the following Nernst Eqn (1),^{36,37}

$$E_{\text{RHE}} = E_{\text{Ag/AgCl}} + E_{\text{Ag/AgCl}}^0 + 0.0591 \text{ V} \times \text{pH} \quad (E_{\text{Ag/AgCl}}^0 = 0.1976 \text{ V vs NHE at } 25^\circ\text{C}) \quad (1)$$

where NHE is the normal hydrogen electrode.

Characterizations

A monochromatic Cu-K α ($\lambda = 0.154$ nm) X-ray diffractometer in conjunction with a Bruker D8 Advance X-ray diffractometer (XRD) was used to identify the crystal structures and phases of the thin films. The high-resolution surface morphology was investigated utilizing an FEI Nova 600 Nanolab focused ion beam-scanning electron microscope (FIB-SEM). A Bruker Innova Atomic Force Microscope (AFM, USA) was also used to assess the surface morphology and roughness of the thin films in a chosen region of $10 \times 10 \mu\text{m}^2$, using RTESP-300 high quality etched silicon probes in a peak force tapping mode. The Nasoscope Analysis v1.7 software (Bruker, USA) was applied to analyse the acquired AFM images. A Thermo Fisher Scientific



NEXSA spectrometer, equipped with a micro-focused monochromatic Al X-ray source (1486.7 eV) with an X-ray spot size of $400 \times 200 \mu\text{m}$, was used to perform the x-ray photoelectron spectroscopy (XPS) and Ultraviolet photoelectron spectroscopy (UPS) analysis. The photoelectron energy shift was calibrated using the C 1s electron at 284.8 eV as the reference point. A PerkinElmer UV-VIS-NIR lambda 1050 spectrophotometer was used to obtain the UV-visible Diffuse Reflectance Spectra (DRS) of the thin films, and the Kubelka-Munk function was used to estimate the bandgap energy associated with each spectrum.

Results and Discussion

The XRD patterns in **Fig. 1a** showed that the thin films—0 g-urea-6C-9mM, 0.1 g-urea-6C-9mM, 0.15 g-urea-6C-9mM and 0.2 g-urea-6C-9mM—exhibited similar diffraction features. Specifically, the peaks at 2θ degree of 20.8° , 27.9° , 29.6° , 30.6° , 32.4° , 33.2° , 34.1° , 37.4° , 46.6° , 52.9° , 53.3° and 55.6° are attributed to the (200), (211), (220), (002), (102), (310), (112), (202), (411), (213), (402), and (332) planes of tetragonal CuBi_2O_4 (PDF#48-1886).^{38,39} In addition, five other peaks at 26.5° , 37.7° , 51.4° , 61.6° , and 65.5° are observed and ascribed to the underlying FTO substrate.⁴⁰ No additional peaks or noticeable shifts were detected upon the usage of the urea, indicating high phase purity of the CuBi_2O_4 thin films.

The crystallite size of the CuBi_2O_4 thin films was estimated based on the (211) facets using the Scherrer equation,⁴¹ as presented in **Fig. 1b**, being 1137, 998, 730, and 997 Å for 0 g-urea-6C-9mM, 0.1 g-urea-6C-9mM, 0.15 g-urea-6C-9mM, and 0.2 g-urea-6C-9mM, respectively. The variation in crystallite size can be attributed to the supersaturation-controlled nucleation and growth kinetics.^{42,43} Although all samples contain identical Bi^{3+} and Cu^{2+} in 100 mL EG, the effective instantaneous supersaturation at the electrode is modulated by urea content.^{42,43} Urea coordinates with $\text{Cu}^{2+}/\text{Bi}^{3+}$ and interacts with the solvent through hydrogen bonding, controlling the rate of ion release during electrodeposition.^{31,32} With 0.15 g urea, this produces a sustained supersaturation, promoting high nucleation density and restricting individual crystallite growth, resulting in the smallest crystallite size (730 Å).^{42,43} Without urea, rapid ion release generates a brief supersaturation spike; although the nucleation barrier is low during the spike, its short duration limits the number of nuclei, leading to large crystallites (1137 Å).^{42,43} At higher urea content (0.2 g), increased viscosity and slower ion diffusion again reduce nucleation, allowing the crystallite to grow larger (997 Å).^{42,43}



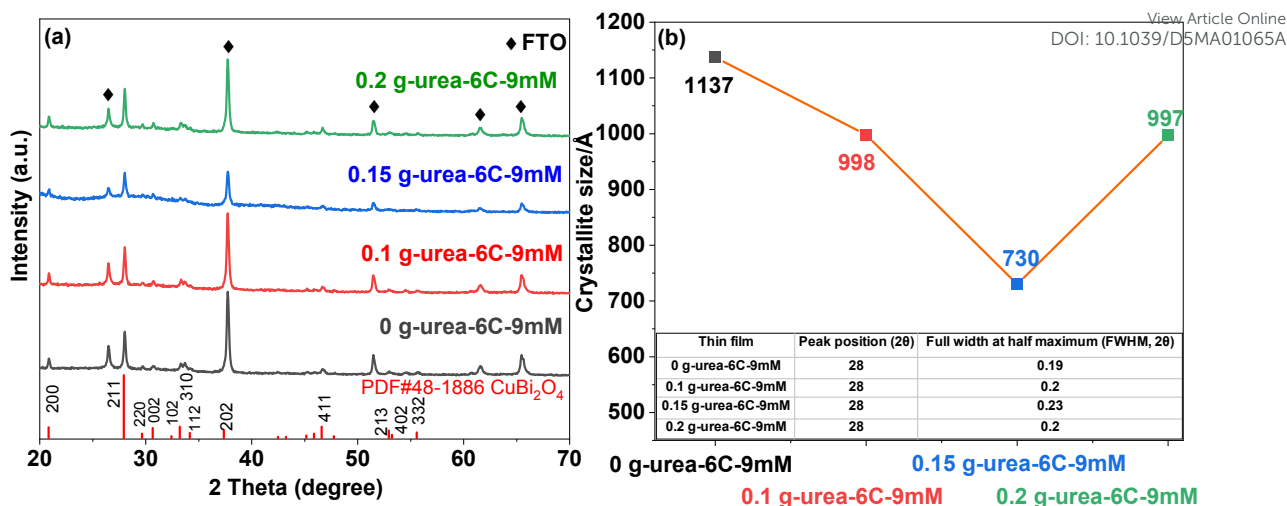


Fig. 1 (a) XRD patterns and (b) corresponding crystallite size of different CuBi₂O₄ thin films deposited on FTO substrate.

The surface morphologies of the CuBi₂O₄ thin films were examined by SEM, with representative low-magnification images shown in **Fig. S3** and high-magnification images in **Fig. 2**. All CuBi₂O₄ thin films exhibit uneven and rough surface features, with some regions containing small nanoparticles, while in others the nanoparticles coalesce into larger branched structures, forming interconnected networks. These networks display irregular, coral-like morphologies reminiscent of finger coral, characterized by pronounced variations in particle size, spatial distribution, and height. The size differences of nanoparticles among the four CuBi₂O₄ thin films were estimated from the particle diameter distribution histograms shown in **Fig. 2**. Specifically, the average diameter of sample without urea (0 g-urea-6C-9mM) is 0.15 μm, whilst being 0.21 and 0.17 μm, respectively, for 0.1 g-urea-6C-9mM and 0.2 g-urea-6C-9mM, being the largest average diameter of 0.24 μm for sample 0.15 g-urea-6C-9mM. This behavior can be understood by combining classical nucleation and growth with non-classical aggregation mechanisms:^{42,43} small crystallites with high surface energy tend to aggregate, forming larger particles. With 0.15 g urea, moderated ion release sustains supersaturation, generating many small crystallites that aggregate in a controlled manner, producing well-packed particles and uniform films. Without or with excess urea, nucleation is limited and aggregation is slowed, resulting in less uniform particles. The low-resolution SEM images in **Fig. S3** further highlight the differences in coral-like interconnected networks distribution, with the urea-containing thin films, especially 0.1 g-urea-6C-9mM and 0.15 g-urea-6C-9mM thin films, showing the most pronounced branched structures.

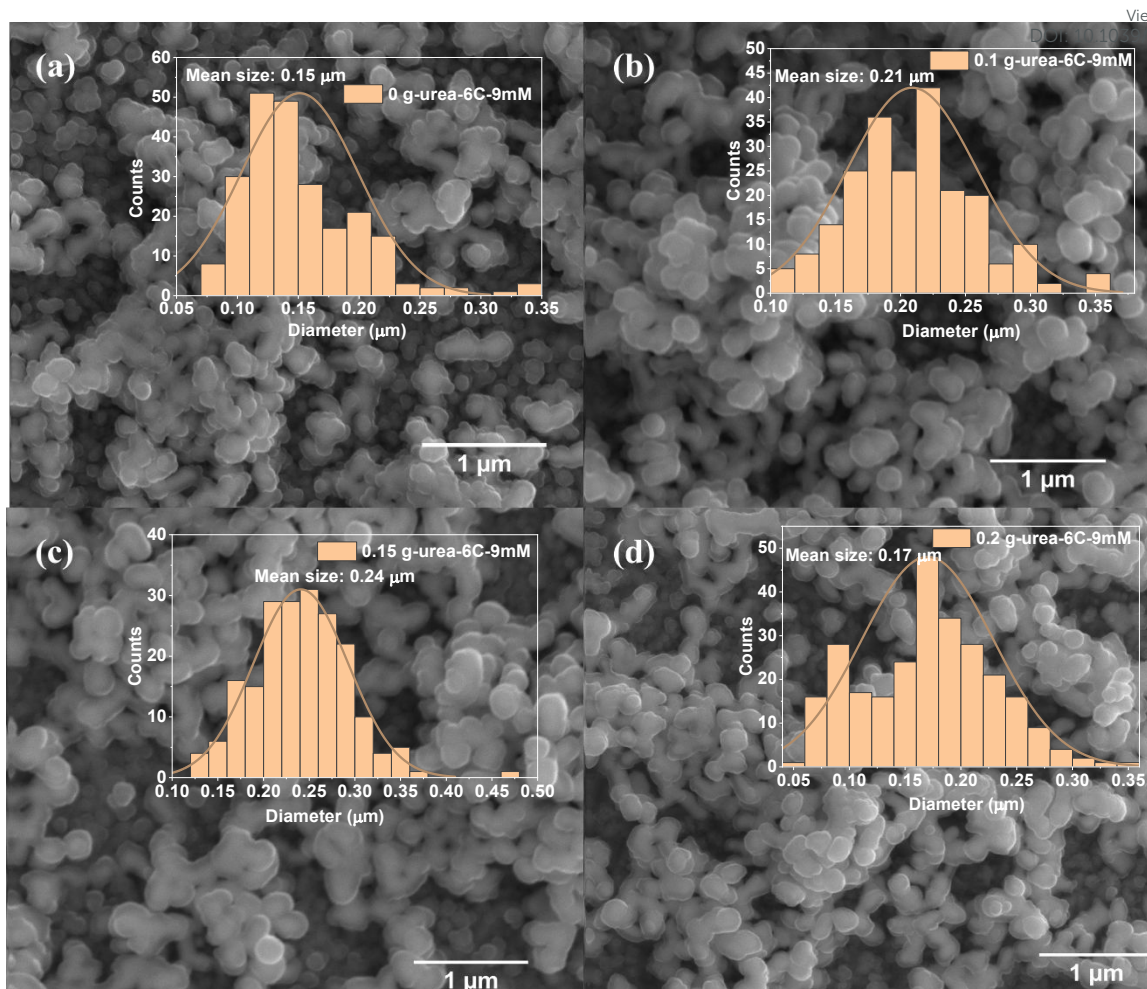


Fig. 2 SEM images of the top view and particle size distribution histograms of the resulting CuBi_2O_4 thin films on FTO substrates: (a) 0 g-urea-6C-9mM; (b) 0.1 g-urea-6C-9mM; (c) 0.15 g-urea-6C-9mM; and (d) 0.2 g-urea-6C-9mM.

The cross-sectional SEM images in **Fig. 3** reveal that all CuBi_2O_4 thin films are composed of nanoparticle aggregates coalesced into porous, irregular networks. Their vertical height of these branched regions varies, and the mean thickness were determined from the thickness histogram in **Fig. 3**. The thin film prepared under urea-free conditions (0 g-urea-6C-9mM) exhibits a moderately compact structure with a mean thickness of $\sim 1.1 \mu\text{m}$. In contrast, films deposited from urea-containing electrolytes display increased thicknesses of $\sim 1.5 \mu\text{m}$ (0.1 g-urea-6C-9mM), $\sim 1.4 \mu\text{m}$ (0.15 g-urea-6C-9mM), and $\sim 1.5 \mu\text{m}$ (0.2 g-urea-6C-9mM). These results show that urea promotes vertical growth by moderating ion release during electrodeposition, which enhances nucleation and aggregation along the vertical direction, leading to thicker, more pronounced branched structures. EDS spectra displayed in **Fig. S4** show that Cu, Bi, O, Sn, Si, and the coated C are present in all thin films. The Cu/Bi atomic ratios of all samples, derived from EDS analysis, are 3.09: 6.39 for 0 g-urea-6C-9mM, 3.49: 7.62 for 0.1 g-urea-6C-





9mM, 9.86: 19.48 for 0.15 g-urea-6C-9mM, and 0.97: 1.94 for 0.2 g-urea-6C-9mM. These values correspond closely to a Cu: Bi ratio of approximately 1: 2, consistent with the stoichiometric composition of CuBi_2O_4 . This result demonstrates the successful synthesis of CuBi_2O_4 thin films, which is consistent with the XRD analysis.

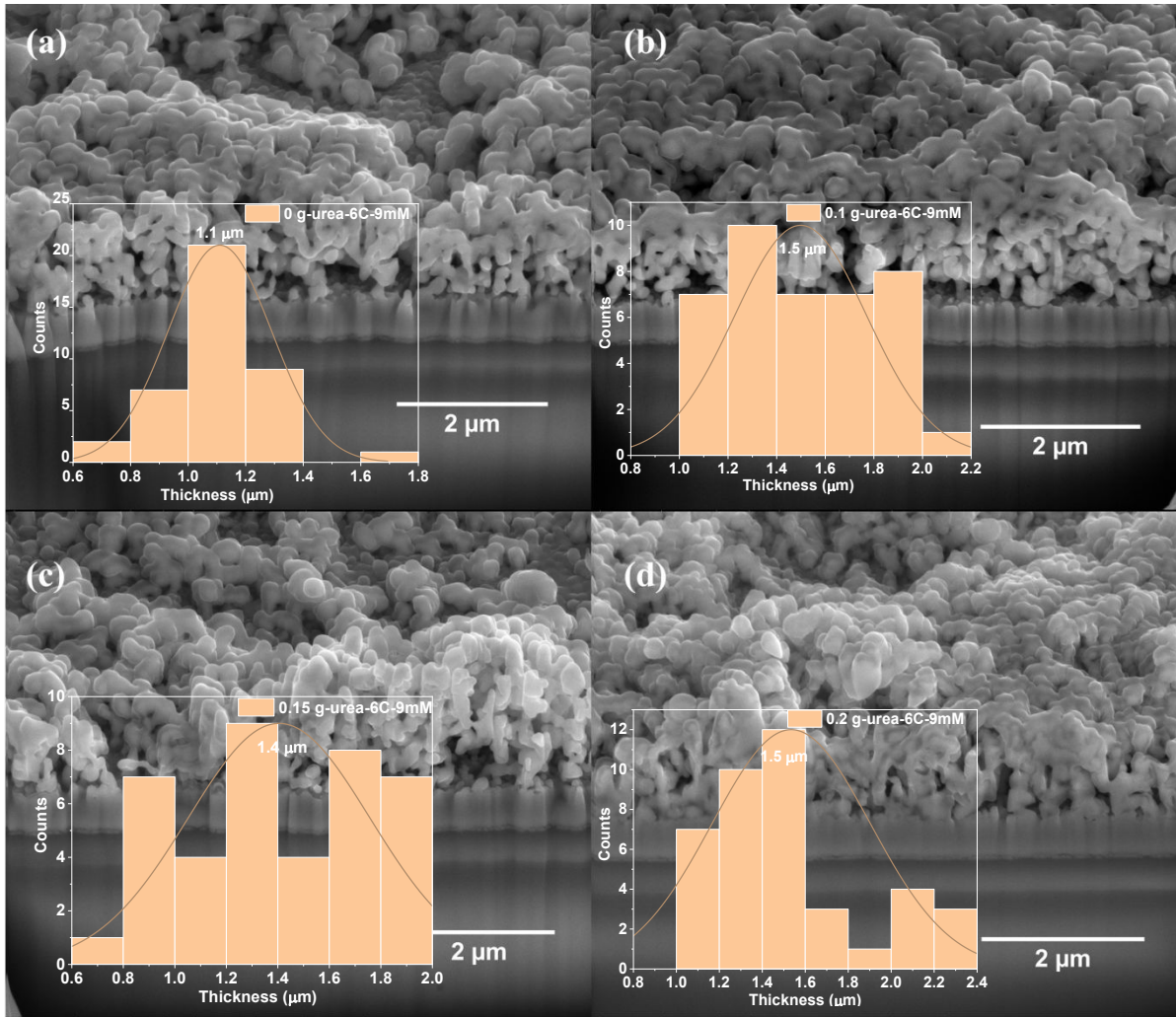


Fig. 3 SEM images of Cross-section views and thickness histograms of the resulting CuBi_2O_4 thin films on FTO substrates: (a) 0 g-urea-6C-9mM; (b) 0.1 g-urea-6C-9mM; (c) 0.15 g-urea-6C-9mM; and (d) 0.2 g-urea-6C-9mM.

Three-dimensional (3D) perspective topographical pictures displayed in **Fig. 4** present the vertical height variations caused by the bumps, pits, or other surface irregularities. The topologies of all the CuBi_2O_4 thin films demonstrate a non-uniform growth, characterized by areas where certain regions grow aggressively into large and high-height features, while other parts exhibit minimal growth. Specifically, thin films of 0.1 g-urea-6C-9mM and 0.15 g-urea-6C-9mM show more uniform distributions of large, high-height regions compared with thin films 0 g-urea-6C-9mM and 0.2 g-urea-6C-9mM. The two-dimensional (2D) views, showing

the height signals along the given section lines, the corresponding mean roughness (R_a), the maximum height (R_{max}) values, and other related parameters, are presented in **Fig. S5**. Where R_{max} is defined as the height difference between the highest and lowest points on the cross-sectional profile relative to the centre line over the length of the profile. The variations in the R_{max} values indicate the non-uniform topology features of the thin films. The surface average R_a values of the CuBi_2O_4 thin films are 181.1 nm for sample 0 g-urea-6C-9mM, 174.9 nm for sample 0.1 g-urea-6C-9mM, sample 0.15 g-urea-6C-9mM for 154.2 nm, and 185.1 nm for 0.2 g-urea-6C-9mM (**Fig. S5**), indicating a more uniform surface for samples 0.1 g-urea-6C-9mM and 0.15 g-urea-6C-9mM.

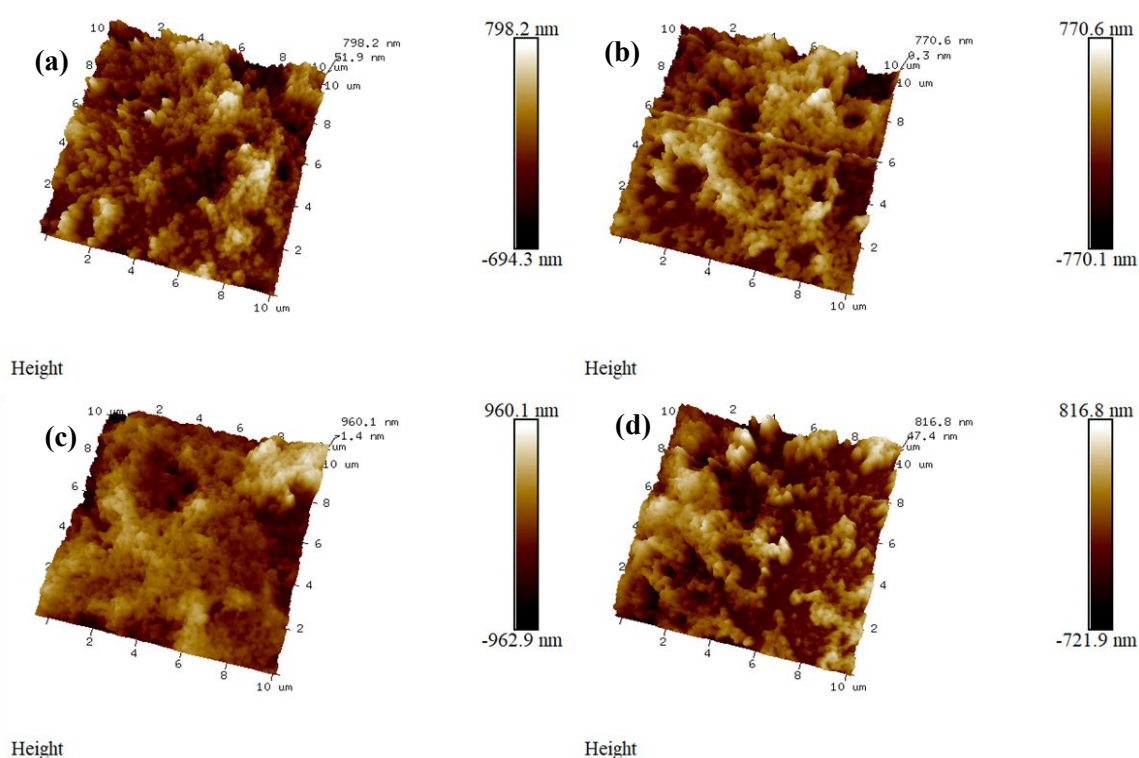


Fig. 4 AFM 3D perspectives of (a) 0 g-urea-6C-9mM, (b) 0.1 g-urea-6C-9mM, (c) 0.15 g-urea-6C-9mM, and (d) 0.2 g-urea-6C-9mM.

According to the XPS survey scan results shown in **Fig. S6**, both samples have similar entire spectra with Cu 2p, Bi 4f, and O 1s peaks. **Fig. 5a** reveals the high-resolution Bi 4f spectra of samples 0 g-urea-6C-9mM and 0.15 g-urea-6C-9mM. The binding energies at 158.6 and 163.9 eV are responsible for the typical spin-orbit split Bi 4f_{7/2} and Bi 4f_{5/2} peaks, respectively, which are brought on by the Bi³⁺ component in both samples.^{44,45} The small peaks fitted at lower binding energies of 162.2 and 156.9 eV are attributed to residual metallic Bi on



the surface of the CuBi_2O_4 lattice.^{46,47} In **Fig. 5b**, the raw data exhibit four peaks: a doublet for Cu 2p and two additional shake-up peaks. These shake-up peaks are attributed to a strong interaction of the final states, involving charge transfer from O 2p band to the Cu 3d band,^{48,49} Cu 2p spectra are typically featured by focusing on the Cu 2p_{3/2} peak and the lower binding energy shake-up peak, owing to their distinctive spectral features that allow for reliable fitting. Peaks with binding energies of 933.9 and 932.3 eV, fitted from the Cu 2p_{3/2} peak, are attributed to the Cu^{2+} in the CuBi_2O_4 lattice and Cu^+ species, respectively.^{44,49} Peaks located at 943.7 and 941.2 eV, obtained from the lower binding energy shake-up peak, further suggest the coexistence of these Cu^{2+} and Cu^+ species within the CuBi_2O_4 thin films. The peak area ratios of Bi^{3+} and Bi (9: 1), as well as that of Cu^{2+} and Cu^+ (8: 2), in the 0.15 g-urea-6C-9mM thin film and 0 g-urea-6C-9mM thin film, are maintained without significant change. This indicates that the addition of urea into the electrolyte during the electrodeposition process does not significantly affect the chemical composition and the chemical states of the CuBi_2O_4 thin film. To further confirm the chemical states and quantify the surface concentration of Cu species in the CuBi_2O_4 thin film, the Cu LM2 Auger spectra were analysed. As depicted in **Fig. 5c**, the Cu LM2 Auger electron spectra show peaks corresponding to the lattice Cu^{2+} (blue peaks) and the low-valence Cu^+ species (red peaks).^{50,51} This finding is consistent with the results obtained from the Cu 2p spectra. The O 1s spectra (**Fig. 5d**) for both CuBi_2O_4 samples were fitted into three distinct peaks at binding energies of approximately 529.4, 530.5, and 531.4 eV. These peaks are attributed to lattice oxygen (O_L),⁵⁰⁻⁵² surface hydroxyl group,^{50,51} and absorbed water species, respectively. The presence of surface hydroxyl groups in CuBi_2O_4 is commonly associated with surface oxygen environments influenced by the coexistence of $\text{Cu}^{2+}/\text{Cu}^+$ states, as observed in the Cu LM2 Auger spectra. The O_L peak area ratios for CuBi_2O_4 thin films of 0 g-urea-6C-9mM and 0.15 g-urea-6C-9mM are 49.5 % and 47.2%, respectively, while the surface hydroxyl species for these two CuBi_2O_4 thin films are 39.3% and 42.1%, respectively. This variation may be attributed to the different distribution of aggregated, finger coral-like structures on the surface of the thin films.



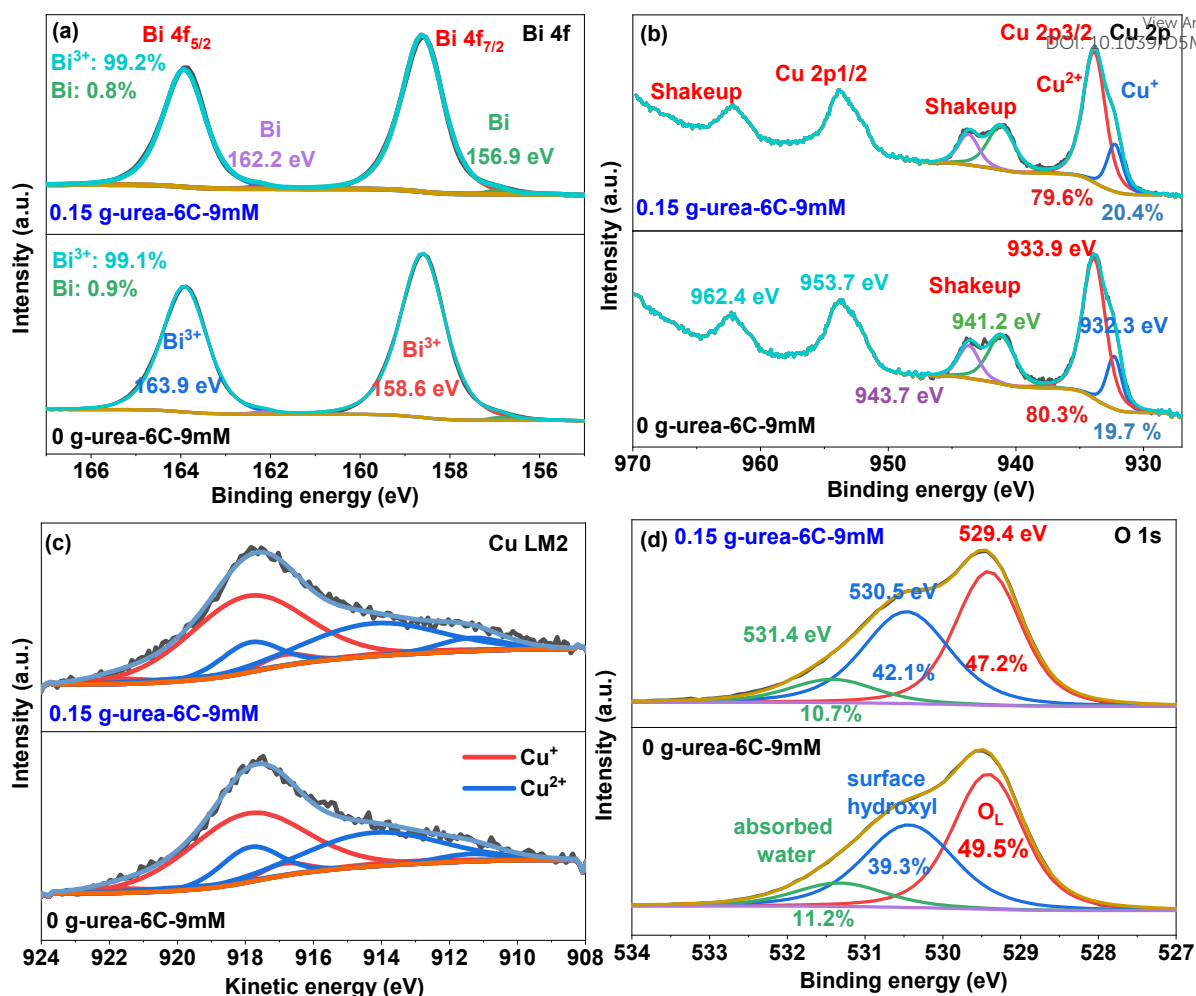


Fig. 5 XPS spectra of prepared CuBi₂O₄ thin films: 0 g-urea-6C-9mM and 0.15 g-urea-6C-9mM. (a) Bi 4f, (b) Cu 2p, (c), Cu LM2, and (d) O 1s.

The UV-visible absorbance spectra (**Fig. 6a**) exhibit strong visible-light absorptions in all thin films. The incident light absorbances of the CuBi₂O₄ thin films: 0.15 g-urea-6C-9mM and 0.2 g-urea-6C-9mM are higher compared with those of 0 g-urea-6C-9mM and 0.1 g-urea-6C-9mM CuBi₂O₄. Slight red shifts can be observed upon introducing 0.15 g and 0.2 g urea into the electrodeposition process. This increase in optical absorption and reduction in reflectance (**Fig. 6b**, inset) are attributed to the varying surface topographical features induced by the urea. **Fig. 6b** presents the direct transition band gap values for the samples—1.88 eV for sample 0 g-urea-6C-9mM, 1.89 eV for sample 0.1 g-urea-6C-9mM, 1.87 eV for sample 0.15 g-urea-6C-9mM, and 1.86 eV for sample 0.2 g-urea-6C-9mM. These values are consistent with those reported in previous studies.¹³

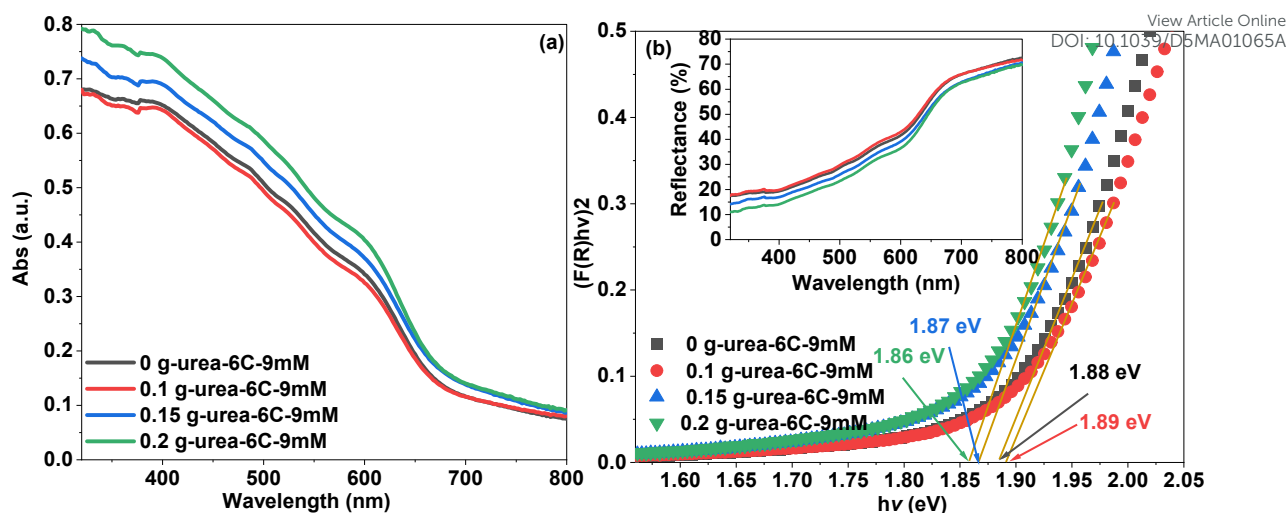


Fig. 6 (a) UV-visible absorbance spectra of the CuBi_2O_4 thin films and (b) the corresponding predicted band gap values from the Kubelka-Munk function,⁵³ with the UV-visible Diffuse Reflectance Spectra (DRS) shown inset.

Mott-Schottky measurements are utilized at 1 kHz in 0.1 M NaOH solution in dark condition, to estimate the flat band potential (E_{fb}) and the hole density (N_A) of the CuBi_2O_4 thin films. The Mott-Schottky plots depicted in **Fig. 7a** were obtained from the following Eqn (2):⁵⁴

$$\frac{1}{C^2} = \frac{2}{A^2 e \epsilon \epsilon_0 N_A} \left(-E + E_{fb} - \frac{KT}{e} \right) \quad (2)$$

where the parameters C , A , E_{fb} , N_A , ϵ , ϵ_0 , and E correspond to the capacitance, the electrode surface area ($1 \times 10^{-4} \text{ m}^2$), the flat-band potential, the acceptor density, the relative permittivity (dielectric constant) of 80 as reported previously,^{54,55} the permittivity of free space ($8.854 \times 10^{-12} \text{ F/m}$),³⁶ and the applied potential, respectively.⁵⁴ As shown in **Fig. 7a**, the corresponding values of the slope and hole densities of the CuBi_2O_4 thin films were calculated and listed in **Table 1**.¹² All the regression lines exhibit negative slopes, indicating that the samples are p-type semiconductor.³⁸ Comparison of the N_A values indicates that all samples exhibit hole densities of the same order of magnitude. Sample 0 g-urea-6C-9mM shows the highest hole density, likely due to the transition from Cu^+ to Cu^{2+} , which releases electrons and thereby enhances the hole density. The flat band potentials of the CuBi_2O_4 thin films are 1.41 V vs. RHE for samples 0 g-urea-6C-9mM and 0.1 g-urea-6C-9mM, and 1.40 V vs. RHE for sample 0.15 g-urea-6C-9mM and sample 0.2 g-urea-6C-9mM, respectively. In p-type



semiconductors, the flat band potential is approximately aligned with the energy level near the valence band edge.⁵⁶ The potential of the conduction band can be determined based on the following Eqn (3).⁵⁷

$$E_c = E_v - E_g \quad (3)$$

The potentials of both the conduction and valence band positions relative to the water redox potential were constructed and illustrated in **Fig. 7b**. The valence band potentials of all the thin films at pH 12.8 are above 1.98 V vs. RHE (corresponding to 1.23 V vs. RHE at pH 0), while the conduction band potentials are above 0.75 V vs. RHE (corresponding to 0 V vs. RHE at pH 0).⁵⁸ Therefore, the CuBi_2O_4 thin films demonstrate the capability to perform the hydrogen evolution reaction under a pH of 12.8. Additionally, the band edge positions differ by only 10 mV, which is within the range of experimental error and would not significantly affect the overall band structure. The ultraviolet photoelectron spectroscopic (UPS) analysis using a He (I) laser ($h\nu = 21.22$ eV) as the incident light was utilized to determine the work functions of the CuBi_2O_4 thin films. As illustrated in **Fig. S7**, the work functions for samples 0 g-urea-6C-9mM and 0.15 g-urea-6C-9mM are 5.03 eV and 5.21 eV, respectively. Therefore, the energy required to extract electrons from the materials differs by a maximum of 0.2 eV, which is quite similar and might not be enough to affect the PEC water splitting performance.

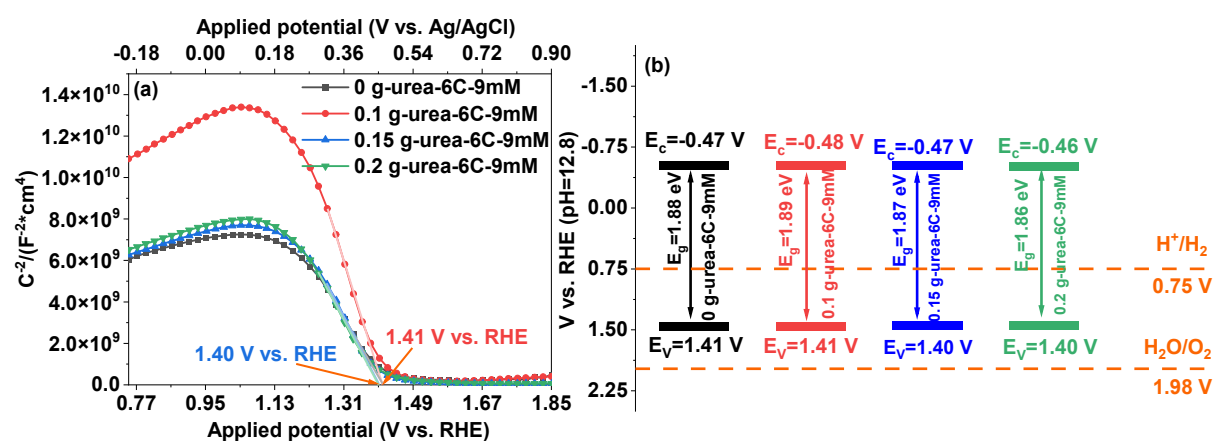


Fig. 7 Mott-Schottky plots (a) and (b) the estimated band structures of the CuBi_2O_4 thin films.



Table 1 Band edge potential position, Mott-Schottky slope value, and corresponding hole densities.

Thin film	Conduction band potential (V vs. RHE)	Valence band potential (V vs. RHE)	the value of the slope	N_A (cm ⁻³)
0 g-urea-6C-9mM	-0.47	1.41	-3.18E10	5.54E19
0.1 g-urea-6C-9mM	-0.48	1.41	-5.94E10	2.97E19
0.15 g-urea-6C-9mM	-0.47	1.40	-3.57E10	4.94E19
0.2 g-urea-6C-9mM	-0.46	1.40	-3.46E10	5.09E19

Open Access Article. Published on 23 December 2025. Downloaded on 12/25/2025 5:51:15 AM.
This article is licensed under a Creative Commons Attribution 3.0 Unported Licence.



The J - V and Nyquist plots are displayed in **Fig. 8**, which were obtained from linear sweeping voltammetry (LSV) and frequency response analyser (FRA) impedance potentiostatic mode, respectively, for the investigation of the PEC performance of the CuBi_2O_4 thin films. In **Fig. 8a**, sample 0 g-urea-6C-9mM exhibits the highest photocurrent density of -0.94 mA/cm² at 0.52 V vs. RHE, whilst the photocurrent density was further improved after the introduction of urea during the electrodeposition process, reaching -1.04 and -1.44 mA/cm² for the 0.1 and 0.15 g urea samples, which is higher than previously published values (**Table S2**). Further increasing the amount of urea to 0.2 g led to a decreased photocurrent density of -0.99 mA/cm², which is still greater than that of sample 0 g-urea-6C-9mM. Therefore, the charge separation and transfer efficiencies have been improved. The Nyquist spectra (**Fig. 8b**) fitted via the following equivalent circuit inserted in the **Fig. 8b** are applied to investigate the charge-transfer resistance of the CuBi_2O_4 thin films. R_s represents the intercept of the semicircle with the real axis ($\text{Re}(Z)$) at low frequency, indicating the resistance of the electrolyte solution and any inherent resistance of the setup. The diameter of the semicircle in the Nyquist plot is utilized to determine the charge transfer resistance (R_{ct}) at the interface of the CuBi_2O_4 thin film and FTO glass. The double-layer capacitance (C_{dl}) represents the capacitive behaviour at the interface, while the Warburg impedance (W) indicates the influence of the diffusion processes on the impedance response in combination with the double-layer capacitance. According to **Fig. 8b** and **Table 2**, sample 0.15 g-urea-6C-9mM, which exhibits the smallest semicircle diameter, has the lowest charge transfer resistances (R_{ct}) with a value

Materials Advances Accepted Manuscript

of 2430 Ω . This is followed by sample 0.2 g-urea-6C-9mM ($R_{ct} = 3193 \Omega$), and sample 0.1 g-urea-6C-9mM ($R_{ct} = 4169 \Omega$), whilst the urea-free reference CuBi_2O_4 thin film exhibits the highest charge transfer resistance of 5441 Ω . Therefore, the charge transfer efficiencies of the CuBi_2O_4 thin films are ranked as follows: 0.15 g-urea-6C-9mM > 0.2 g-urea-6C-9mM > 0.1 g-urea-6C-9mM > 0 g-urea-6C-9mM under the bias of 0.52 V vs. RHE. The C_{dl} values, however, exhibit an opposite trend, with the 0.15 g-urea-6C-9mM thin film showing the highest C_{dl} value. This implies a larger area for charge separation, potentially enhancing the PEC performance. The observed decrease in charge transfer resistance, coupled with the increased C_{dl} , indicates an improved efficiency in utilizing photogenerated charges for these thin films.

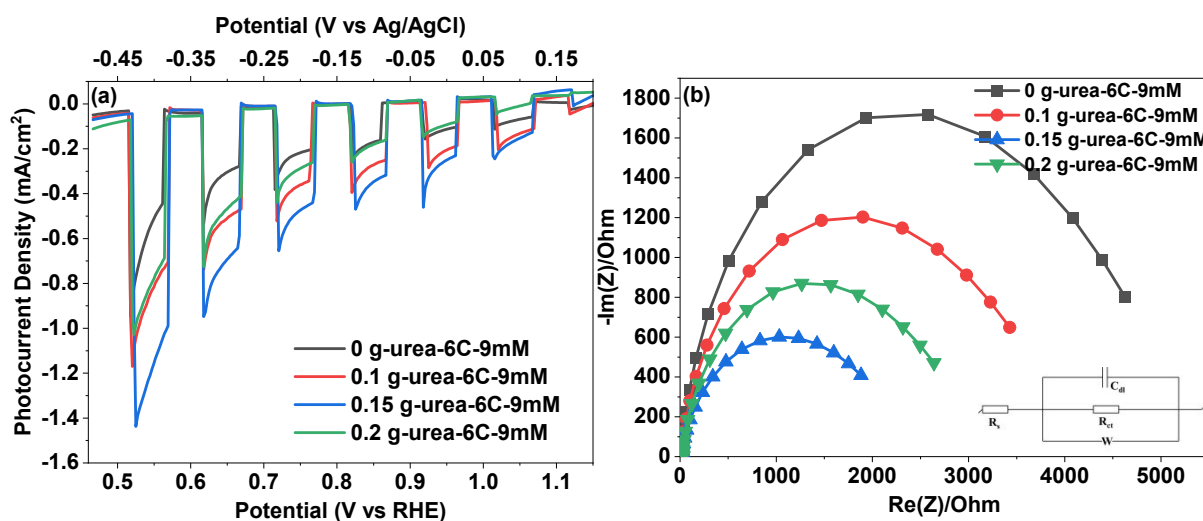


Fig. 8 (a) Photocurrent density-potential vs. RHE or Ag/AgCl (J - V) plots under chopped illumination condition, (b) EIS Nyquist plots obtained at -0.45 V vs. Ag/AgCl under one sun simulated light illumination.

Table 2 parameters: R_s , R_{ct} , C_{dl} , and W obtained from the fitted Nyquist plots of the CuBi_2O_4 thin films.

	0 g-urea-6C-9mM	0.1 g-urea-6C-9mM	0.15 g-urea-6C-9mM	0.2 g-urea-6C-9mM
R_s	26.22 Ω	23.06 Ω	20.75 Ω	25.31 Ω
R_{ct}	5441 Ω	4169 Ω	2430 Ω	3193 Ω
C_{dl}	15.26 μF	16.58 μF	18.29 μF	15.25 μF



<i>W</i>	14593 Ω·s ^{-0.5}	9099 Ω·s ^{-0.5}	3925 Ω·s ^{-0.5}	6932 Ω·s ^{-0.5}
----------	---------------------------	--------------------------	--------------------------	--------------------------

View Article Online
DOI: 10.1039/D5MA01065A

The stability of the CuBi₂O₄ thin films has been investigated using I-t curves measured through chronoamperometry under continuous solar light illumination for 2 h at 0.52 V vs. RHE. Thin film 0.15 g-urea-6C-9mM, which exhibits the highest photocurrent density, was used to investigate the stability performance in comparison to thin film 0 g-urea-6C-9mM. As shown in **Fig. S8**, both thin films showed poor PEC stabilities. Specifically, initial sharp drops in photocurrent density were observed within approximately 10 seconds. After 100 seconds of continuous illumination, both films reached their steady-state photocurrents, with sample 0.15 g-urea-6C-9mM exhibiting approximately -0.27 mA/cm², which is about 42% higher than the reference (-0.19 mA/cm²).

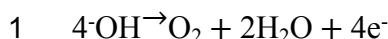
The variations in PEC performance (photocurrent density and photostability) of the CuBi₂O₄ thin films can be primarily attributed to the urea-induced morphological differences. Examination of the charge-time curves (**Fig. S9**) recorded during electrodeposition reveals that the presence of urea slows the deposition process under the same applied charges. This effect arises from the coordination of urea with Cu²⁺ and Bi³⁺ ions, which stabilizes them in solution and maintains a steady concentration of electroactive species.^{59,60} This behavior further supports the sustained-supersaturation condition proposed earlier, which governs both the nucleation rate and subsequent particle aggregation. Under the influence of urea, the resulting more continuous particle networks and slightly increased film thickness provide more efficient charge-transport pathways and reduce recombination at interparticle boundaries, accounting for the higher photocurrent densities of the urea-assisted thin films. Moreover, the improved structural coherence and uniformity help to moderate photocorrosion, explaining the modest enhancement in stability compared to the referent thin film (0 g-urea-6C-9mM).

Based on above analyses, a possible charge separation and transfer mechanism has been proposed to explain the improved PEC water splitting performance. As illustrated in **Fig. 9**, under solar light illumination, the CuBi₂O₄ thin film generates photocarriers after absorbing light with energy greater than its band gap. A built-in electric field separates the photo-generated electrons and holes. Ideally, the electrons will transfer to the surface of the CuBi₂O₄ thin film to participate in the reduction reaction Eqn (4):⁶¹



Meanwhile, the Pt counter electrode serves as the site for the oxidation reaction Eqn (5):⁶¹





(5)

The generated electrons at the counter electrode flow through the external circuit back to the CuBi_2O_4 thin film, completing the electrical circuit. However, an undesirable photocorrosion reaction occurs within the CuBi_2O_4 thin film due to the insufficiently anodic valence band potential of the synthesized CuBi_2O_4 photocathode (1.4 V vs. RHE at pH 12.8). This thermodynamic limitation prevents the efficient oxygen evolution reaction (OER), leading to the photogenerated holes oxidizing the CuBi_2O_4 lattice and degrading the Cu-O-Bi framework into CuO and Bi_2O_3 rather than driving water oxidation (1.98 V vs. RHE at pH 12.8).⁶²⁻⁶⁴ Furthermore, in an alkaline electrolyte, Bi^{3+} within the CuBi_2O_4 lattice reacts with hydroxide ions to form soluble hydroxo complexes,⁶² leading to the bismuth leaching effect and structural destabilization. Simultaneously, Cu^+ species undergo the following disproportionation Eqn (6):⁶³



(6)

where the resulting Cu^{2+} species react with hydroxide ions to form hydroxy complexes,⁶³ which further accelerates the lattice degradation. The residual photocurrent remains due to the presence of surviving CuBi_2O_4 domains and the photoactivity of the secondary phases.

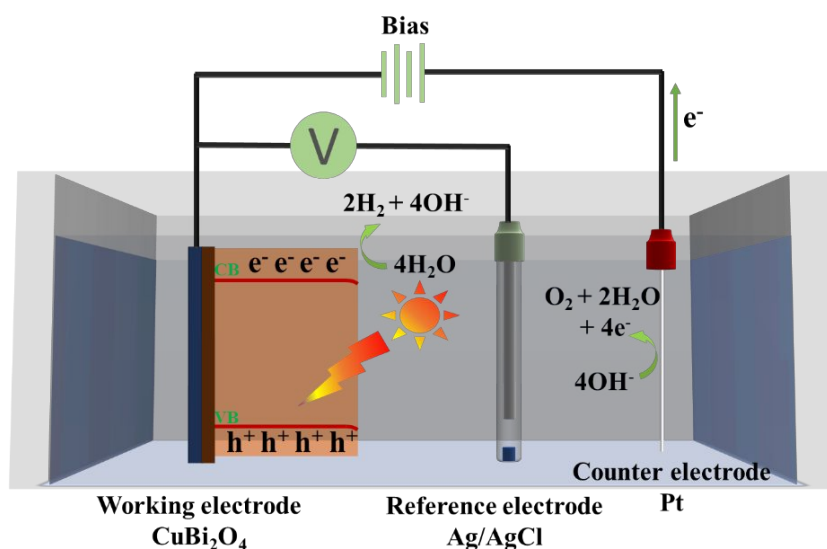


Fig. 9 Schematic illustration of the electronic transfer under the possible mechanism.

Conclusions

This work successfully developed a CuBi_2O_4 photocathode with an interconnected nanoparticle textured morphology for PEC water splitting. AFM characterization showed that the CuBi_2O_4 thin film prepared with 0.15 g urea per 100 mL of EG exhibited the lowest surface roughness and best uniformity compared with thin films prepared with other urea concentrations. XPS analyses revealed that the element composition and chemical states, as well as the electronic band structures observed through electrochemical characterization, remained largely unchanged. This indicated that the variations of urea in the EG electrolyte primarily contributed to the physical differences, such as crystallite size, uniformity and thickness, rather than affecting the chemical performance. Durability tests demonstrated that, after 100 seconds of continuous illumination, the 0.15 g-urea-6C-9mM CuBi_2O_4 thin film stabilized at approximately -0.27 mA/cm^2 , while the 0 g-urea-6C-9mM CuBi_2O_4 thin film stabilized at -0.19 mA/cm^2 . This represents a 42% enhancement in stability for the 0.15 g-urea-6C-9mM CuBi_2O_4 thin film, which is attributed to its more uniform morphology. These findings underscore the introduction of urea into the EG electrolyte enhances the uniformity and performance of CuBi_2O_4 thin film, thereby improving their effectiveness in PEC water splitting applications.



View Article Online
DOI: 10.1039/D5MA01065A

1 **Conflict of interests**

2 The authors declare that they have no known competing financial interests or personal
3 relationships that could have appeared to influence the work reported in this paper.
4



1 **Data availability**

View Article Online
DOI: 10.1039/D5MA01065A

- 2 All data supporting the findings of this study are included within the article and its Electronic
3 Supplementary Information (ESI).
4



Acknowledgements

A. A. Tahir and Y. Zhu acknowledge the Engineering and Physical Sciences Research Council (EPSRC), UK, under research grant numbers EP/T025875/1 and EP/V049046/1. The author X. Yang would like to acknowledge the financial support from the University of Exeter-China Scholarship Council PhD Scholarship. The authors would also like to thank Dr. Shaoliang Guan of the University of Cardiff for his effort to the XPS equipment support. For the purpose of open access, the authors have applied a Creative Commons Attribution (CC BY) licence to any Author Accepted Manuscript version arising from this submission



References

1. Y. H. Lee, J. Kim and J. Oh, *ACS Appl. Mater. Interfaces*, 2018, 10, 33230-33237, <https://doi.org/10.1021/acsami.8b10943>.
2. S. Masudy-Panah, R. S. Moakhar, C. S. Chua, A. Kushwaha, T. I. Wong and G. K. Dalapati, *RSC Adv.*, 2016, 6, 29383-29390, <https://doi.org/10.1039/c6ra03383k>.
3. J. Luo, L. Steier, M.-K. Son, M. Schreier, M. T. Mayer and M. Grätzel, *Nano Lett.*, 2016, 16, 1848-1857, <https://doi.org/10.1021/acs.nanolett.5b04929>.
4. G. S. Pawar, A. Elikkotttil, S. Seetha, K. S. Reddy, B. Pesala, A. A. Tahir and T. K. Mallick, *ACS Appl. Energy Mater.*, 2018, 1, 3449-3456, <https://doi.org/10.1021/acsaeem.8b00628>.
5. Q. Cai, Z. Liu, C. Ma, Z. Tong and C. Han, *J. Mater. Sci.: Mater. Electron.*, 2018, 29, 20629-20638, <https://doi.org/10.1007/s10854-018-0201-z>.
6. R.-P. Li, S.-M. Yu and Z.-Y. Zhao, *Mater. Chem. Phys.*, 2024, 311, 128582, <https://doi.org/10.1016/j.matchemphys.2023.128582>.
7. W. Yang, S. Lee, H. C. Kwon, J. Tan, H. Lee, J. Park, Y. Oh, H. Choi and J. Moon, *ACS Nano*, 2018, 12, 11088-11097, <https://doi.org/10.1021/acs.nano.8b05446>.
8. P. R. Narangari, J. D. Butson, H. H. Tan, C. Jagadish and S. Karuturi, *Nano Lett.*, 2021, 21, 6967-6974, <https://doi.org/10.1021/acs.nanolett.1c02205>.
9. N. Guijarro, M. S. Prevot and K. Sivula, *J. Phys. Chem. Lett.*, 2014, 5, 3902-3908, <https://doi.org/10.1021/jz501996s>.
10. D. Kang, J. C. Hill, Y. Park and K.-S. Choi, *Chem. Mater.*, 2016, 28, 4331-4340, <https://doi.org/10.1021/acs.chemmater.6b01294>.
11. S. P. Berglund, F. F. Abdi, P. Bogdanoff, A. Chemseddine, D. Friedrich and R. van de Krol, *Chem. Mater.*, 2016, 28, 4231-4242, <https://doi.org/10.1021/acs.chemmater.6b00830>.
12. Y. Xu, J. Jian, F. Li, W. Liu, L. Jia and H. Wang, *J. Mater. Chem. A*, 2019, 7, 21997-22004, <https://doi.org/10.1039/c9ta07892d>.
13. S. Wei, N. Xu, F. Li, X. Long, Y. Hu, L. Gao, C. Wang, S. Li, J. Ma and J. Jin, *ChemElectroChem*, 2019, 6, 3367-3374, <https://doi.org/10.1002/celec.201900714>.
14. N. W. Kim, B. U. Choi, H. Yu, S. Ryu and J. Oh, *Opt. Express*, 2019, 27, A171-A183, <https://doi.org/10.1364/OE.27.00A171>.
15. T. Chtouki, M. El Mrabet, A. Tarbi, I. Goncharova and H. Erguig, *Opt. Mater.*, 2021, 118, 111294, <https://doi.org/10.1016/j.optmat.2021.111294>.
16. J. Yu, W. Han, A. A. Suleiman, S. Han, N. Miao and F. C. Ling, *Small Methods*, 2024, 8, 2301282, <https://doi.org/10.1002/smtd.202301282>.



- 1 17. J. Lee, H. Yoon, S. Kim, S. Seo, J. Song, B. U. Choi, S. Y. Choi, H. Park, S. Ryu, J. Oh
2 and S. Lee, *Chem. Commun.*, 2019, 55, 12447-12450, <https://doi.org/10.1039/c9cc06092h>.
3 18. R. Garg, S. Gonuguntla, S. Sk, M. S. Iqbal, A. O. Dada, U. Pal and M. Ahmadipour, *Adv.*
4 *Colloid Interface Sci.*, 2024, 330, 103203, <https://doi.org/10.1016/j.cis.2024.103203>.
5 19. B. Duployer, C. Tenailleau, Y. Thimont, P. Lenormand, A. Barnabé and L. Presmanes,
6 *Mater. Res. Bull.*, 2020, 130, 110940, <https://doi.org/10.1016/j.materresbull.2020.110940>.
7 20. S. Shahidi, B. Moazzenchi and M. Ghoranneviss, *Eur. Phys. J. Appl. Phys.*, 2015, 71, 31302,
8 <https://doi.org/10.1051/epjap/2015140439>.
9 21. B. Meena, M. Kumar, R. K. Hocking, S. Juodkazis, V. Biju, P. Subramanyam and C.
10 Subrahmanyam, *Energy Fuels*, 2023, 37, 14280-14289,
11 <https://doi.org/10.1021/acs.energyfuels.3c00731>.
12 22. F. C. Krebs, *Sol. Energy Mater. Sol. Cells*, 2009, 93, 394-412,
13 <https://doi.org/10.1016/j.solmat.2008.10.004>.
14 23. F. Wang, A. Chemseddine, F. F. Abdi, R. van de Krol and S. P. Berglund, *J. Mater. Chem.*
15 *A*, 2017, 5, 12838-12847, <https://doi.org/10.1039/c7ta03009f>.
16 24. D. Perednis and L. J. Gauckler, *J. electroceram.*, 2005, 14, 103-111,
17 <https://doi.org/10.1007/s10832-005-0870-x>.
18 25. T. H. V. Nguyen, C.-H. Wu, S.-Y. Lin and C.-Y. Lin, *J. Taiwan Inst. Chem. Eng.*, 2019,
19 95, 241-251, <https://doi.org/10.1016/j.jtice.2018.07.010>.
20 26. C.-Y. Lin, S.-Y. Lin, M.-C. Tsai and C.-H. Wu, *Sustain. Energy Fuels*, 2020, 4, 625-632,
21 <https://doi.org/10.1039/c9se00558g>.
22 27. N. T. Hahn, V. C. Holmberg, B. A. Korgel and C. B. Mullins, *J. Phys. Chem. C*, 2012, 116,
23 6459-6466, <https://doi.org/10.1021/jp210130v>.
24 28. E. Kalinina and E. Pikalova, *Materials*, 2021, 14, 5584,
25 <https://doi.org/10.3390/ma14195584>.
26 29. Y. Nakabayashi, M. Nishikawa and Y. Nosaka, *Electrochim. Acta*, 2014, 125, 191-198,
27 <https://doi.org/10.1016/j.electacta.2014.01.088>.
28 30. A. Al-Osta, B. S. Samer, U. T. Nakate, V. V. Jadhav and R. S. Mane, *Microelectronic*
29 *Engineering*, 2020, 229, 111359, <https://doi.org/10.1016/j.mee.2020.111359>.
30 31. M. G. Weldehans, T. T. K. Ngan, T. T. Salunkhe and I. T. Kim, *J. Mater. Chem. A*, 2025,
31 DOI: 10.1039/d5ta07895d, <https://doi.org/10.1039/d5ta07895d>.
32 32. H.-S. Kim, R. Verma, J. Kim and C.-J. Park, *ACS Sustainable Chem. Eng.*, 2020, 8, 11123-
33 11132, <https://doi.org/10.1021/acssuschemeng.0c01513>.
34 33. S. M. Paradine, *Tetrahedron*, 2025, 184, <https://doi.org/10.1016/j.tet.2025.134781>.



- 1 34. D. Piecha, J. Kapusta-Kołodziej, M. M. Marzec, K. Sokołowski, M. Kozieł and A. Brzózka, *Appl. Surf. Sci.*, 2025, 713, 164330, <https://doi.org/10.1016/j.apsusc.2025.164330>.
- 2
- 3 35. T. Wu, J. Kim, Y. H. Choa and N. V. Myung, *Front. Chem.*, 2025, 13, 1635084,
- 4 <https://doi.org/10.3389/fchem.2025.1635084>.
- 5 36. M. Alhabrabi, S. Nundy, A. Ghosh and A. A. Tahir, *ACS Omega*, 2022, 7, 28396-28407,
- 6 <https://doi.org/10.1021/acsomega.2c02996>.
- 7 37. M. Alruwaili, A. Roy, S. Nundy and A. A. Tahir, *RSC Adv.*, 2022, 12, 34640-34651,
- 8 <https://doi.org/10.1039/d2ra05894d>.
- 9 38. L. Zhao, X. Wang and Z. Liu, *Appl. Phys. A*, 2018, 124, 836,
- 10 <https://doi.org/10.1007/s00339-018-2262-5>.
- 11 39. J. Lee, H. Yoon, K. S. Choi, S. Kim, S. Seo, J. Song, B. U. Choi, J. Ryu, S. Ryu, J. Oh, C.
- 12 Jeon and S. Lee, *Small*, 2020, 16, e2002429, <https://doi.org/10.1002/smll.202002429>.
- 13 40. K.-H. Park and M. Dhayal, *RSC Adv.*, 2015, 5, 33503-33514,
- 14 <https://doi.org/10.1039/c4ra15704d>.
- 15 41. K. D. Malviya, H. Dotan, D. Shlenkevich, A. Tsyganok, H. Mor and A. Rothschild, *J.*
- 16 *Mater. Chem. A*, 2016, 4, 3091-3099, <https://doi.org/10.1039/c5ta07095c>.
- 17 42. O. Ait Layachi, A. Moujib and E. m. Khomri, *Electroanal.*, 2024, 36,
- 18 <https://doi.org/10.1002/elan.202400115>.
- 19 43. J. Lin, M. Kilani, M. Baharfar, R. Wang and G. Mao, *Nanoscale*, 2024, 16, 19564-19588,
- 20 <https://doi.org/10.1039/d4nr02389g>.
- 21 44. X. Wang, W. Liu, C. Wang, S. Zhang, M. Ding and X. Xu, *Sens. Actuators B: Chem.*, 2021,
- 22 344, 130190, <https://doi.org/10.1016/j.snb.2021.130190>.
- 23 45. F. Wang, H. Yang and Y. Zhang, *Mater. Sci. Semicond. Process.*, 2018, 73, 58-66,
- 24 <https://doi.org/10.1016/j.mssp.2017.09.029>.
- 25 46. J. Wang, L. Tang, G. Zeng, Y. Liu, Y. Zhou, Y. Deng, J. Wang and B. Peng, *ACS*
- 26 *Sustainable Chem. Eng.*, 2016, 5, 1062-1072, <https://doi.org/10.1021/acssuschemeng.6b02351>.
- 27 47. S. Yu, H. Huang, F. Dong, M. Li, N. Tian, T. Zhang and Y. Zhang, *ACS Appl. Mater.*
- 28 *Interfaces*, 2015, 7, 27925-27933, <https://doi.org/10.1021/acsami.5b09994>.
- 29 48. J. Ghijsen, L. H. Tjeng, J. van Elp, H. Eskes, J. Westerink, G. A. Sawatzky and M. T.
- 30 Czyzyk, *Phys. Rev. B.*, 1988, 38, 11322-11330, <https://doi.org/10.1103/physrevb.38.11322>.
- 31 49. HarwellXPS, HARWELLXPS GURU,
- 32 <https://www.harwellxps.guru/xpskb/copper/#1755794343725-850aaad2-863d>, (accessed 10th
- 33 September, 2025).



- 1 50. M. C. Biesinger, *Surf. Interface Anal.*, 2017, 49, 1325-1334, <https://doi.org/10.1002/sia.6239>.
2
- 3 51. M. C. Biesinger, L. W. M. Lau, A. R. Gerson and R. S. C. Smart, *Appl. Surf. Sci.*, 2010,
4 257, 887-898, <https://doi.org/10.1016/j.apsusc.2010.07.086>.
- 5 52. L. Qu, R. Tan, A. Sivanantham, M. J. Kang, Y. J. Jeong, D. H. Seo, S. Kim and I. S. Cho,
6 *J. Energy Chem.*, 2022, 71, 201-209, <https://doi.org/10.1016/j.jechem.2022.03.013>.
- 7 53. S. Sharma and N. Khare, *Colloid Polym. Sci.*, 2018, 296, 1479-1489,
8 <https://doi.org/10.1007/s00396-018-4362-3>.
- 9 54. F. Wang, W. Septina, A. Chemseddine, F. F. Abdi, D. Friedrich, P. Bogdanoff, R. van de
10 Krol, S. D. Tilley and S. P. Berglund, *J. Am. Chem. Soc.*, 2017, 139, 15094-15103,
11 <https://doi.org/10.1021/jacs.7b07847>.
- 12 55. M. Li, X. Tian, X. Zou, X. Han, C. Du and B. Shan, *Int. J. Hydrog. Energy*, 2020, 45,
13 15121-15128, <https://doi.org/10.1016/j.ijhydene.2020.03.242>.
- 14 56. N. Hoang Lam, N. Tam Nguyen Truong, K.-S. Ahn, Y. Jo, S. Beom Kang, N. Huu Hieu,
15 S. F. Shaikh, C.-D. Kim, M. Lee and J. Hak Jung, *FlatChem*, 2024, 43, 100600,
16 <https://doi.org/10.1016/j.flatc.2023.100600>.
- 17 57. S. Huang, G. Wang, J. Liu, C. Du and Y. Su, *ChemCatChem*, 2020, 12, 4431-4445,
18 <https://doi.org/10.1002/cctc.202000634>.
- 19 58. A. Kudo and Y. Miseki, *Chem. Soc. Rev.*, 2009, 38, 253-278,
20 <https://doi.org/10.1039/b800489g>.
- 21 59. M. Mouanga, L. Ricq and P. Berçot, *J. Appl. Electrochem.*, 2007, 38, 231-238,
22 <https://doi.org/10.1007/s10800-007-9430-1>.
- 23 60. S. Survilienė, O. Nivinskienė, A. Češunienė and A. Selskis, *J. Appl. Electrochem.*, 2006,
24 36, 649-654, <https://doi.org/10.1007/s10800-005-9105-8>.
- 25 61. W. Xue, J. Tian, X. Hu, J. Fan, T. Sun and E. Liu, *Chem. Eng. J.*, 2022, 443, 136427,
26 <https://doi.org/10.1016/j.cej.2022.136427>.
- 27 62. S. Zhang, M. Rohloff, O. Kasian, A. M. Mingers, K. J. J. Mayrhofer, A. Fischer, C. Scheu
28 and S. Cherevko, *J. Phys. Chem. C*, 2019, 123, 23410-23418,
29 <https://doi.org/10.1021/acs.jpcc.9b07220>.
- 30 63. M. G. De Chialvo, J. Zerbino, S. Marchiano and A. Arvia, *J. appl. electrochem.*, 1986, 16,
31 517-526, <https://doi.org/10.1007/BF01006847>.
- 32 64. H. Khan, M.-J. Kim, P. Balasubramanian, M.-J. Jung and S.-H. Kwon, *Cell Rep. Phys. Sci.*,
33 2023, 4, 101652, <https://doi.org/10.1016/j.xcrp.2023.101652>.
- 34



Data availability

[View Article Online](#)
DOI: 10.1039/D5MA01065A

All data supporting the findings of this study are included within the article and its Electronic Supplementary Information (ESI).

